Friedrich, A., Winkler, B., Morgenroth, W., Ruiz-Fuertes, J., Koch-Müller, M., Rhede, D., Milman, V. (2014): Pressure-induced spin collapse of octahedrally coordinated Fe3+ in Ca3Fe2[SiO4]3 from experiment and theory. - *Physical Review B*, *90*, 9

DOI: http://doi.org/10.1103/PhysRevB.90.094105

PHYSICAL REVIEW B **90**, 094105 (2014)

Pressure-induced spin collapse of octahedrally coordinated Fe^{3+} in $Ca_3Fe_2[SiO_4]_3$ from experiment and theory

Alexandra Friedrich,[*] Björn Winkler, Wolfgang Morgenroth, and Javier Ruiz-Fuertes
Institut für Geowissenschaften, Goethe-Universität, Altenhöferallee 1, D-60438 Frankfurt a.M., Germany

Monika Koch-Müller
GFZ Potsdam, Sektion 3.3, Telegrafenberg, 14473 Potsdam, Germany

Dieter Rhede
GFZ Potsdam, Sektion 4.2, Telegrafenberg, 14473 Potsdam, Germany

Victor Milman
Dassault Systèmes BIOVIA, 334 Science Park, Cambridge CB4 0WN, United Kingdom

(Received 9 April 2014; revised manuscript received 11 August 2014; published 5 September 2014)

The high-pressure behavior of andradite garnet, $Ca_3Fe_2[SiO_4]_3$, was studied at pressures up to 80 GPa using single-crystal synchrotron x-ray diffraction, Raman spectroscopy, and quantum mechanical calculations based on density functional theory. An isosymmetric phase transition was observed in the pressure range between 60 and 70 GPa, which is associated with a gradual high-spin to low-spin electronic transition in Fe^{3+}. Experimental structural data before and after the phase transition are in excellent agreement with the theoretically predicted structural compression of the high-spin and low-spin phases, respectively. While the overall unit-cell volume is reduced by about 2.5% across the phase transition, a collapse of about 10% of the FeO_6 octahedral volume is observed, attributed to the reduced Fe–O bond lengths associated with low-spin Fe^{3+}. In combination with earlier data the present study shows that a spin collapse of Fe^{3+} in FeO_6 octahedra will be triggered if the Fe–O bond length reaches a critical value of $d(\text{Fe–O}) < \approx 1.9$ Å. Earlier reported results for the compressibility of the cation coordination polyhedra are substantially revised, with $B_{FeO_6} = 195(2)$ GPa, $B_{CaO_8} = 104(2)$ GPa, and $B_{SiO_4} = 348(11)$ GPa for the high-spin phase. The mode Grüneisen parameters range between 0.61 and 1.34. The computed spin-pairing energy is $\approx$4.2 eV at 0 GPa.

DOI: 10.1103/PhysRevB.90.094105 PACS number(s): 61.50.Ks, 61.05.cp, 71.15.Mb, 78.30.−j

I. INTRODUCTION

Iron is the most abundant transition metal, and due to their electronic structures, both Fe^{2+} and Fe^{3+} ions may undergo spin-pairing transitions at high pressures. Such pressure-induced spin transitions have already been predicted by Fyfe [1] and high-pressure experiments allowed to obtain experimental evidence for these electronic transitions in $Fe_{0.94}O$ [2], hematite, Fe_2O_3 [3,4], and FeS [5] using Mössbauer spectroscopy and x-ray emission spectroscopy (XES).

Garnets play an important role in nature and technology. They are important minerals of the Earth's mantle, used in jewelry, and crystals with the garnet structure are fabricated for laser, magnetic, and ion-conducting technologies [6]. A pressure-induced magnetic collapse and spin transition accompanied by a Mott transition has been observed in synthetic yttrium iron garnet (YIG), $Y_3Fe_5O_{12}$, at 48 GPa [7,8]. $Y_3Fe_5O_{12}$ is a well-known magnetic garnet with wide application in electronic devices. Magnetic garnets are used as magneto-optical isolators and in microwave technology as magnetic resonance filters, tuned oscillators, and band-reject and band-pass filters [6]. In $Y_3Fe_5O_{12}$, Fe^{3+} occupies octahedral and tetrahedral sites of the garnet structure. However, as the high-pressure phase of $Y_3Fe_5O_{12}$ was amorphous [7,9], the structural changes due to the HS-LS transition could not be evaluated.

Andradite, $Ca_3Fe_2[SiO_4]_3$, is a garnet end member with Fe^{3+} in octahedral coordination. Like the majority of garnets, it crystallizes in space group $Ia\bar{3}d$, where all the cations occupy fully-constrained special positions (Fig. 1). The high symmetry of the garnet structure and of the cation coordinations make andradite an ideal model system to study pressure-induced spin-pairing transitions of Fe^{3+} in octahedral coordination. Specifically, the spin-pairing behavior in andradite may serve as a benchmark for that of iron-bearing magnesium silicate perovskite, $(Mg_{1-x}Fe_x)SiO_3$, where spin transitions of iron have been extensively studied [10] and a spin-pairing transition in Fe^{3+} located on the octahedral B site was controversially proposed at pressures of 13–24 GPa [11] or 50–60 GPa [12]. Several high-pressure studies have already been conducted on andradite up to 36 GPa [13–17]. No structural phase transition has been reported so far. In the present study we report on a pressure-induced spin transition in andradite from single-crystal x-ray diffraction, Raman spectroscopy and quantum mechanical calculations based on density-functional theory.

II. METHODS

A. Experimental details

Andradite single crystals were synthesized from a stoichiometric mixture of synthetic $Ca(OH)_2$, Fe_2O_3, and SiO_2 with OH in excess to promote crystal growth, sealed within

---

[*] friedrich@kristall.uni-frankfurt.de

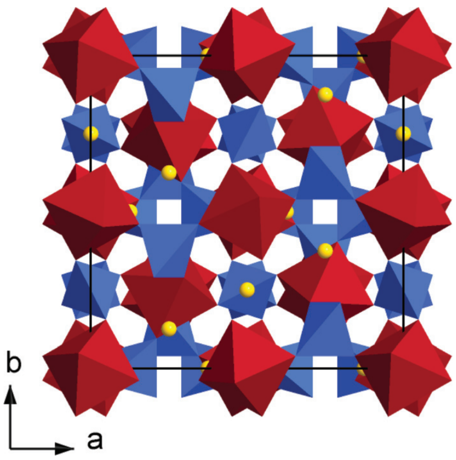

FIG. 1. (Color online) Crystal structure of andradite. FeO_6 octahedra (red) and SiO_4 tetrahedra (blue) share corners in a three-dimensional framework. Ca atoms (yellow spheres) occupy triangular dodecahedral sites.

a platinum capsule, at 3 GPa and 1273 K in a multianvil press using the 18/11 assembly according to the experimental design given in Koch-Müller et al. [18]. The chemical composition was determined by wavelength-dispersive x-ray analysis (WDS) techniques using a JEOL JXA-8500F (HYPERPROBE) electron microprobe. Natural and synthetic reference standards were diopside (for Mg, Si, and Ca), hematite (for Fe), and orthoclase (for Al).

Several grains of garnets were embedded in UV glue, ground and polished on both sides to thicknesses ranging from 35 to 136 μm for FTIR investigations. Unpolarized FTIR spectra were obtained at the synchrotron IR beamline at BESSY II (Berlin, Germany) using a Nicolet 870 FTIR spectrometer (with KBr beamsplitter) combined with a Continuum microscope and a MCT detector. The aperture was set to $12 \times 12\ \mu\text{m}^2$. The spectra were collected with a resolution of 2 cm^{-1} and averaged over 256 scans. As no molar absorption coefficient ε for andradite has been reported so far, we used the IR calibration of Bell et al. [19] for two pyrope-rich garnets ($6700 \pm 670\,\text{l}\,\text{mol}^{-1}_{\text{H}_2\text{O}}\,\text{cm}^{-2}$) for quantification. For the high-pressure experiments small single crystals of andradite ($\leqslant$25 μm diameter and $\leqslant$8 μm thickness) were loaded together with ruby chips for pressure determination [20] and neon as a pressure-transmitting medium into holes of $\approx$85 μm diameter in rhenium gaskets preindented to thicknesses of $\leqslant$30 μm in Boehler-Almax diamond anvil cells equipped with conical diamonds (250 and 200 μm culet sizes) [21].

Single-crystal synchrotron x-ray diffraction was performed at the Extreme Conditions Beamline P02.2 at PETRA III, Hamburg, Germany ($\lambda = 0.28968$ Å, beam size 2.4(H) × 2.1(V) μm^2) [22]. Diffraction images were collected on compression at various pressures up to 77 GPa (except for the data at 70 GPa, which were collected after decompression from 73.5 GPa) with a PerkinElmer XRD 1621 flat-panel detector at a sample-to-detector distance of 399.82 mm by 1° ω scanning. A smaller scan range than the cell opening was used at the two lowest pressures due to a displacement of the ω-rotation axis from the synchrotron beam, which was then realigned, and at 70 and 77 GPa due to the limited availability of synchrotron beam time (Table I). The image format was converted according to the procedure described by Rothkirch et al. [23] for further processing with the $CrysAlis^{Pro}$ software Agilent [24] for indexing Bragg reflections, intensity data reduction, and empirical absorption correction. Crystal structures were refined with SHELXL97-2 [25], operated using the WinGX interface [26]. The final refinement was carried out with anisotropic displacement parameters for all atoms. The Ca:Fe ratio was refined for the triangular dodecahedral site with the constraint that the sum of the occupancies of Ca and Fe was fixed to one. An extinction correction was applied for one of the crystals (No. 1). The polyhedral volumes were calculated with the program IVTON [27]. Experimental details, crystal data and refinement results are summarized in Table I.

Micro-Raman measurements were performed with a Renishaw Raman spectrometer (RM-1000) equipped with a CCD detector and a green Nd:YAG-laser (532 nm, 200 mW). We employed a nonconfocal geometry and a 20× objective lens with a long-working distance. The sample was one of the two single crystals (crystal No. 1) which had been used for single-crystal x-ray diffraction and pressurized to about 78 GPa. Raman spectra were measured after the diffraction experiments during decompression to ambient pressure in the range from 100 to 1300 cm^{-1}. All spectra were corrected by subtracting a background and fitted to Lorentzian functions using the program DatLab [28].

B. Computational details

The quantum-mechanical calculations were performed based on density functional theory (DFT) for a pure andradite end-member composition $Ca_3Fe_2^{3+}[SiO_4]_3$ using the program *CASTEP* [29]. The calculations were performed with the on-the-fly pseudopotentials from the *CASTEP* database using a kinetic cutoff energy of 800 eV and a $4 \times 4 \times 4$ Monkhorst-Pack grid [30], yielding distances $\leqslant$0.03 Å^{-1} between sampling points of the reciprocal lattice. The Wu-Cohen [31] exchange-correlation functional was employed.

The high-spin (HS) and the low-spin (LS) structures represent local minima in the total energy hypersurface. Hence, we chose the corresponding formal spin states as starting values, but allowed full spin relaxation after a few SCF cycles. The results were then analyzed by a Mulliken population analysis and invariably showed either the HS or LS state. The use of other starting configurations also led to either the HS or LS state, and attempts to model to an intermediate spin state while not fixing the spin failed.

III. RESULTS

A. Composition of the synthetic garnets

The product of the synthesis in the multianvil press consists of reddish isomorphic single crystals in size ranging from submicron to about 200 μm. Optical inspection in transmitted light as well as microprobe analyses reveal that two different populations of garnets have been grown: a nearly pure andradite end member, $(Ca_{2.88}Mg_{0.07}Fe^{2+}_{0.04})(Fe^{3+}_{1.96}Al_{0.04})Si_3O_{12}$, with lighter red color and andradite with 7 mole% skiagite component, $(Ca_{2.71}Fe^{2+}_{0.21}Mg_{0.03})(Fe^{3+}_{1.97}Al_{0.03})Si_3O_{12}$, with darker red color. See Supplemental Material [32] for a table of the

TABLE I. Details of the data collections, refinement results, and structural data for andradite $Ca_3Fe_2[SiO_4]_3$ at high pressures and ambient temperature. $Z = 8$, space group $Ia\bar{3}d$, $\lambda = 0.28968$ Å.

p (GPa)	3.17(3)	9.49(7)	19.74(9)	27.27(3)	39.20(3)	55.5(2)	59.80(8)	64.68(8)	69.94(9)	73.47(8)	77.0(1)
a (Å)	11.9424(5)	11.8018(5)	11.6172(3)	11.5012(3)	11.3340(4)	11.1535(9)	11.0952(4)	11.0151(13)	10.8980(15)	10.8681(15)	10.8378(7)
crystal No.	1	1	1	1	1	2	1	2	2	2	1
cell opening (°)	66	66	66	66	66	46	66	46	46	46	66
ω-scan range (°)	33	33	66	66	66	46	66	46	40	46	40
$\sin\theta_{max}/\lambda$ (Å^{-1})	1.054	1.067	1.079	1.063	1.064	1.016	1.080	1.001	0.986	1.014	1.068
observed refl.	2063	2029	3761	3639	3554	1563	3274	1373	1111	1275	2117
unique refl., u.r.	530	516	547	533	511	270	490	253	226	240	426
u. r. $[I > 2\sigma(I)]$	415	414	471	451	417	173	415	151	144	142	358
parameters	19	19	19	19	19	18	19	18	18	18	19
$R(int)(F^2)$	0.0766	0.0846	0.0445	0.0416	0.1047	0.0725	0.0365	0.0584	0.0603	0.0756	0.0355
$R(\sigma)$	0.0564	0.0611	0.0252	0.0231	0.0525	0.0466	0.0210	0.0372	0.0426	0.0539	0.0248
$R1$ $[I > 2\sigma(I)]$	0.0449	0.0470	0.0386	0.0369	0.0420	0.0447	0.0371	0.0527	0.0462	0.0518	0.0407
$wR2$	0.1119	0.1170	0.0880	0.0878	0.1045	0.1060	0.0874	0.1730	0.1306	0.1183	0.1080
GoF	1.091	1.102	1.121	1.086	1.087	1.041	1.124	1.139	1.036	0.980	1.127
$\Delta\rho_{max}$ (e Å^{-3})	1.218	1.231	0.957	0.845	0.816	0.584	0.962	0.883	0.674	0.748	0.939
$\Delta\rho_{min}$ (e Å^{-3})	−1.595	−2.573	−2.340	−2.290	−1.569	−0.752	−1.816	−0.974	−0.580	−0.900	−1.900
Occ. (Ca)	0.919(6)	0.912(6)	0.918(4)	0.914(5)	0.911(5)	0.89(1)	0.923(5)	0.88(2)	0.89(2)	0.88(2)	0.914(7)
Occ. (Fe^{2+} on Ca site)	0.081(6)	0.088(6)	0.082(4)	0.086(5)	0.089(5)	0.11(1)	0.077(5)	0.12(2)	0.11(2)	0.12(2)	0.086(7)
x (O)	0.03897(5)	0.03882(6)	0.03866(4)	0.03853(4)	0.03843(5)	0.03822(15)	0.03804(5)	0.0379(2)	0.0377(2)	0.0376(2)	0.03743(7)
y (O)	0.04966(6)	0.05132(6)	0.05323(4)	0.05441(4)	0.05595(5)	0.05825(15)	0.05799(5)	0.0585(2)	0.0567(2)	0.0570(2)	0.05667(7)
z (O)	0.65541(6)	0.65526(6)	0.65503(4)	0.65502(4)	0.65485(5)	0.65429(15)	0.65472(5)	0.6543(2)	0.6517(2)	0.6512(2)	0.65131(7)
U_{eq} (Ca) (Å^2)	0.0063(2)	0.0048(2)	0.0040(1)	0.0051(1)	0.0056(1)	0.0095(2)	0.0052(1)	0.0105(4)	0.0097(3)	0.0101(3)	0.0051(2)
U_{eq} (Fe) (Å^2)	0.0045(2)	0.0036(2)	0.0033(1)	0.0046(1)	0.0053(1)	0.0094(3)	0.0052(1)	0.0104(4)	0.0093(4)	0.0093(3)	0.0044(2)
U_{eq} (Si) (Å^2)	0.0032(2)	0.0020(2)	0.0022(1)	0.0037(1)	0.0045(2)	0.0081(3)	0.0045(1)	0.0094(5)	0.0087(4)	0.0082(4)	0.0040(2)
U_{eq} (O) (Å^2)	0.0069(2)	0.0062(2)	0.0054(1)	0.0064(1)	0.0071(2)	0.0116(4)	0.0066(2)	0.0125(6)	0.0114(5)	0.0118(4)	0.0066(2)
$d_{Fe–O}$ (Å) 4×	2.0032(7)	1.9835(7)	1.9565(4)	1.9408(5)	1.9162(6)	1.8882(16)	1.8812(5)	1.865(2)	1.812(2)	1.803(2)	1.7975(8)
$d_{Si–O}$ (Å) 6×	1.6381(7)	1.6283(7)	1.6142(4)	1.6044(5)	1.5899(6)	1.5807(18)	1.5693(5)	1.564(3)	1.560(2)	1.562(2)	1.5562(8)
$d_{Ca–O}$ (Å) 4×	2.3371(7)	2.3141(7)	2.2835(5)	2.2632(5)	2.2353(6)	2.2051(18)	2.1918(5)	2.174(2)	2.162(2)	2.156(2)	2.1495(8)
$d_{Ca–O}$ (Å) 4×	2.4643(7)	2.4156(7)	2.3556(5)	2.3186(5)	2.2675(6)	2.2081(17)	2.1967(5)	2.179(2)	2.166(2)	2.159(2)	2.1532(8)
Si-O-Fe (°)	132.64(4)	131.69(4)	130.60(3)	129.89(3)	129.02(3)	127.76(10)	127.77(3)	127.54(14)	129.04(13)	128.94(13)	129.04(5)

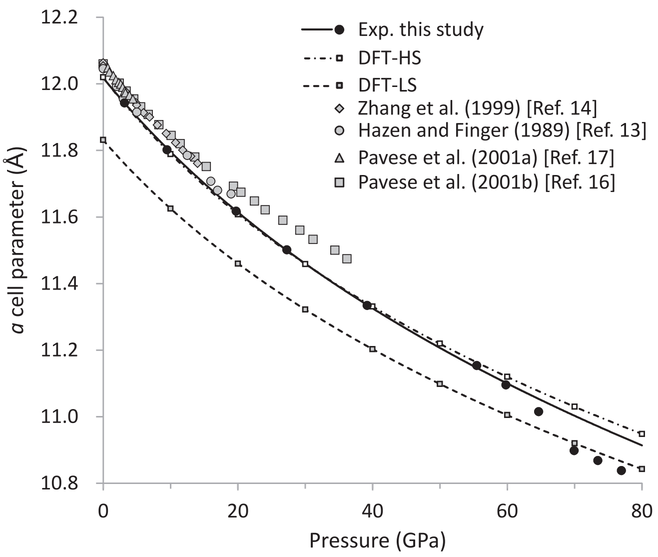

FIG. 2. Unit-cell compression of andradite obtained from single-crystal x-ray diffraction (XRD) (Exp., black dots) and from DFT calculations for the high-spin (HS) and low-spin (LS) configurations. At pressures between 60 and 70 GPa the HS-LS transition is observed. The pressure point at 70 GPa was measured on decompression. Lines represent equation of state fits to the *p-a* data. Literature values from single-crystal XRD [13,14] and powder XRD [16,17] are shown for comparison. Error bars are smaller than the symbol size.

results from electron microprobe analyses. The Fe^{3+}/Fe^{2+} ratio was adjusted assuming full occupancy of the eight cation sites. The two small garnet crystals used for the high-pressure studies turned out to be of the darker-red garnet population. The skiagite component in andradite, i.e., the Fe^{2+} content on the Ca position, was refined from the x-ray diffraction data to 8–9 mole% and 11–12 mole% in crystals No. 1 and 2, respectively (Table I).

The water content in natural andradite garnets varies over a wide range from 0.01 up to 6% by weight [33,34]. The infrared spectra measured on the synthetic andradite in this study showed the typical absorption features for OH in andradite with a maximum at about 3600 cm^{-1} and a flatter tail to the low energy side similar to the natural sample CITH3110 investigated by Amthauer and Rossman [33]. We determined the integral absorbance of ten different crystals, normalized them to equal thickness, and quantified the water content to be 0.06 wt% using the integrated molar absorption coefficient ε_{int} of Bell et al. [19] and the density of 3.92 g/cm^3 as determined in this study for ambient conditions.

B. Compression at low pressures

Our unit-cell data obtained by high-pressure single-crystal x-ray diffraction are systematically lower by 0.1–0.4 % than literature data [13,14,16,17] (Fig. 2). The smaller unit-cell parameter can be explained by the incorporation of 7–12 mole% skiagite component (Fe^{2+} on the Ca site) in the investigated samples. However, the pressure dependence of the cell parameter is similar to the literature data up to about 19 GPa. Discrepancies with the data by Pavese et al. [16] at pressures above 15 GPa cannot be attributed to the skiagite component in our samples, as skiagite is less compressible than andradite (Table II), but are probably due to their use of powder samples and nitrogen as pressure medium, which is less hydrostatic than neon above 15 GPa (Fig. 2).

TABLE II. Overall and polyhedral bulk moduli, B (given in GPa) of andradite and skiagite (Ref. Woodland et al. [48]). V_0 is the unit-cell volume at ambient pressure and is a fit parameter in all cases where errors are given. B' is the pressure derivative of B.

Ref.	V_0 (Å^3)	B	B'	B_{CaO_8}	B_{FeO_6}	B_{SiO_4}
Exp.-HS	1736(2)	161(4)	3.7(2)	104(2)	195(2)	348(11)
DFT-HS	1736.1(4)	151.9(5)	4.48(2)	100(4)	184(1)	343(3)
DFT-LS	1655.9(3)	168.9(5)	4.50(2)	120(3)	198.2(8)	350(3)
DFT [38]	1753.2	147.1(4)	4.41	105	183	327
Exp. [13]	1747.6	159(2)	4	160	330	200
Exp. [14]	1751.3	162(5)	4.7(7)			
Exp. [14]	1751.3	157(1)	5.1			
Exp. [17]	1754(1)	159(3)	5.7(2)			
Exp. [48]	1612.1(3)	157(3)	6.7(8)			
Exp. [48]	1612.1(3)	168(2)	4			

C. Spin transition

Single-crystal x-ray diffraction data show a pressure-induced isosymmetric phase transition in andradite commencing at about 60 GPa and finishing at below 70 GPa as is indicated by a drop of the unit-cell volume of about 2.5% (Fig. 2). From *ab initio* calculations based on DFT a pressure-induced HS-LS transition in Fe^{3+} was predicted in andradite. The experimentally observed pressure dependence of the unit-cell parameter is in excellent agreement with the predicted compression behavior of the HS and LS phases (Fig. 2). This leads to the conclusion that the observed phase transition is due to a HS-LS transition in Fe^{3+}. DFT calculations for an intermediate spin (IS) state of Fe^{3+}, where $S = \frac{3}{2}$, always converged to a HS or LS state, and hence it is unlikely that an IS phase is formed at the phase transition. The deviation of the experimental cell parameter at 64.7 GPa from the extrapolated equation of state of the HS phase indicates that the HS-LS transition in andradite occurs gradually over a pressure range of 5–15 GPa (Fig. 2). At 70 GPa, andradite definitely is present in the LS configuration. From the differences of the enthalpies of the HS and LS configuration the transition pressure was predicted to be about 36 GPa from calculations. It is well known that the theoretical spin-transition pressure strongly depends on the choice of the exchange-correlation functional and the use of a Hubbard U [35,36]. Preliminary calculations, in which a Hubbard $U = 2.5$ eV for the Fe was employed, gave a spin transition pressure of 56 GPa, which agrees better with our observations. However, as it was not the aim of the study to reproduce the experimental value after the observation, but rather predict and explain the pressure-induced spin transition, we did not carry out further DFT calculations with various exchange-correlation functionals and Hubbard parameters.

Our single-crystal data allow us to follow the transition in detail. The volume collapse at the spin transition is much more pronounced in the $Fe^{3+}O_6$ octahedra (with nearly 10% decrease) than in the overall compression (Fig. 3). Again, the

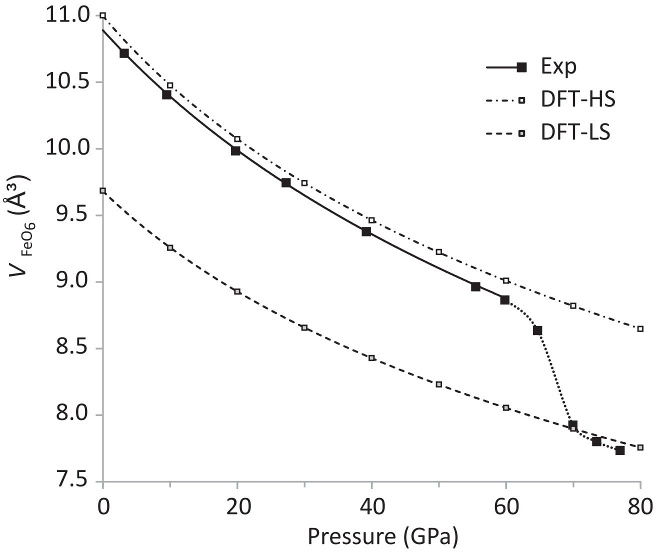

FIG. 3. Polyhedral volume compression of the FeO_6 octahedra in andradite obtained from experiment (Exp) (black dots) and from DFT calculations for the high-spin (HS) and low-spin (LS) configurations. A distinct volume drop is observed between 60 and 70 GPa, which is clearly associated with the HS-LS transition as concluded from the excellent agreement with the theoretical calculations. The pressure point at 70 GPa was measured on decompression. Lines represent equation of state fits to the data. For the experimental data, a guide to the eye has been added for pressures larger than 60 GPa (dotted line). Errors are smaller than the symbol size.

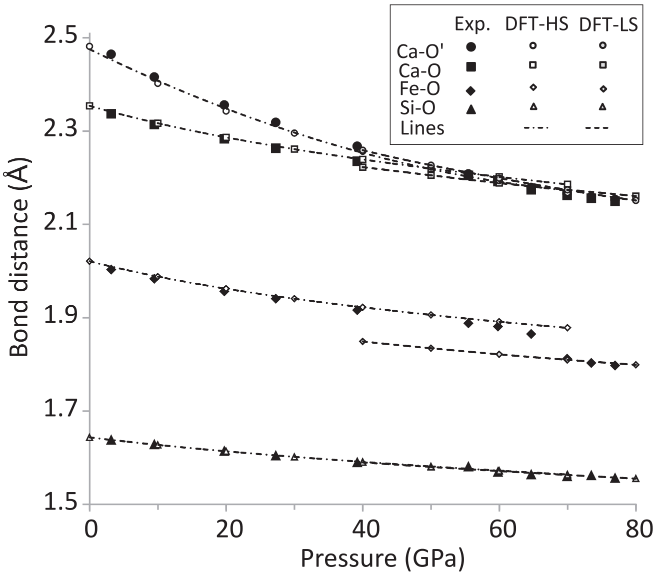

FIG. 4. Compression of the interatomic bond distances in andradite obtained from experiment (Exp) (filled symbols) and DFT (open symbols for HS and gray filled symbols for LS configuration). The two distinct Ca–O bond distances are equal within uncertainties above 50 GPa. The decrease of the Fe–O bond distance between 60 and 70 GPa is associated with the HS-LS transition in Fe^{3+}. The Si–O bond is not affected by the spin transition. Lines are guides to the DFT-HS (dashed dotted lines) and DFT-LS (dashed lines) data. Errors are smaller than the symbol size.

agreement with the calculated octahedral volume compression of the HS and LS phases is excellent and shows that the phase transition observed experimentally is clearly associated with the HS-LS transition in Fe^{3+}. As both single crystals remained optically transparent and orange colored across the phase transition up to the highest pressure obtained, a transition to a metallic state can be excluded as the driving force for the volume collapse.

In contrast to the large volume collapse in the FeO_6 octahedra, the bond distances in the SiO_4 tetrahedra and CaO_8 triangular dodecahedra do not show any distinct changes at the phase transition (Fig. 4). The two symmetrically independent Ca–O bond distances become equal within uncertainties already in the HS phase at about 55 GPa (Fig. 4). They remain similar on further pressure increase up to the maximal pressure obtained (Fig. 4). This behavior can be described by the bond length distortion (BLD) of the polyhedron:

$$BLD(\%) = \frac{100}{n} \sum_{i=1}^{n} \frac{|d_i - \langle d \rangle|}{\langle d \rangle},$$

where d_i is the bond length and $\langle d \rangle$ is the average bond length in the polyhedron [37]. The bond length distortion of the CaO_8 triangular dodecahedron decreases to nearly zero % on pressure increase to about 55.5 GPa, and then remains close to zero % across the spin transition and in the LS phase up to at least 77 GPa. The angular distortion of the SiO_4 tetrahedron shows a slight, continuous decrease on pressure increase without observable discontinuity at the spin transition.

The edge length distortion (ELD) describes the distortion of the FeO_6 octahedron and is characterized by

$$ELD(\%) = \frac{100}{n} \sum_{i=1}^{n} \frac{|OO_i - \langle OO \rangle|}{\langle OO \rangle},$$

where OO_i is the edge length of the polyhedron and $\langle OO \rangle$ is the average edge length [37]. In an earlier theoretical study it was predicted that the edge length distortion of FeO_6 in andradite decreases on pressure increase until it is minimal at about 30 GPa before it increases again but with a changed sense of distortion [38]. From our current calculations, the minimum of the distortion is predicted at a lower pressure of about 10 GPa. This is in excellent agreement with our experimental data, where the minimum is observed between 10 and 15 GPa (Fig. 5). This result clearly shows that the initial pressure-induced change of the FeO_6 octahedral distortion is not associated with the pressure-induced spin transition. At the spin transition the edge length distortion of the FeO_6 octahedron is discontinuously reduced (Fig. 5).

The pressure-induced spin transition is also clearly reflected in the high-pressure Raman spectra of andradite by the appearance of three broad bands occurring at about 610, 770, and 1050 cm^{-1} in the LS phase at 64.8 to 77.8 GPa (Fig. 6). Raman spectra were measured on decompression. At pressures below 71 GPa the intensity of the three broad bands starts to decrease and finally vanishes at about 62.7 GPa (Fig. 6). This behavior indicates that there is no large hysteresis of the phase transition and that the spin transition occurs gradually over a pressure range of at least 5 GPa. We cannot currently

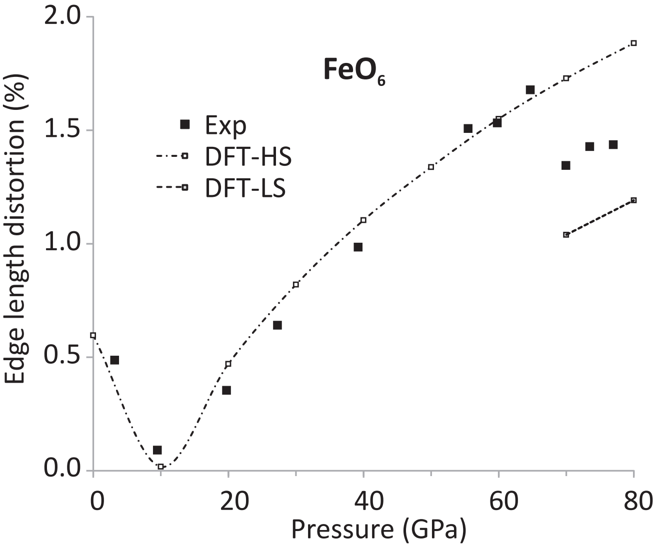

FIG. 5. Pressure dependence of the edge length distortion (ELD) in FeO$_6$. The minimum of the ELD at around 10 GPa has already been predicted in an earlier theoretical study at a higher pressure of about 30 GPa [38] and is not associated with the spin transition. At pressures larger than 60 GPa the ELD is strongly reduced due to the spin transition. In this pressure region, the agreement with theory is not as outstanding, but the difference is small on an absolute scale.

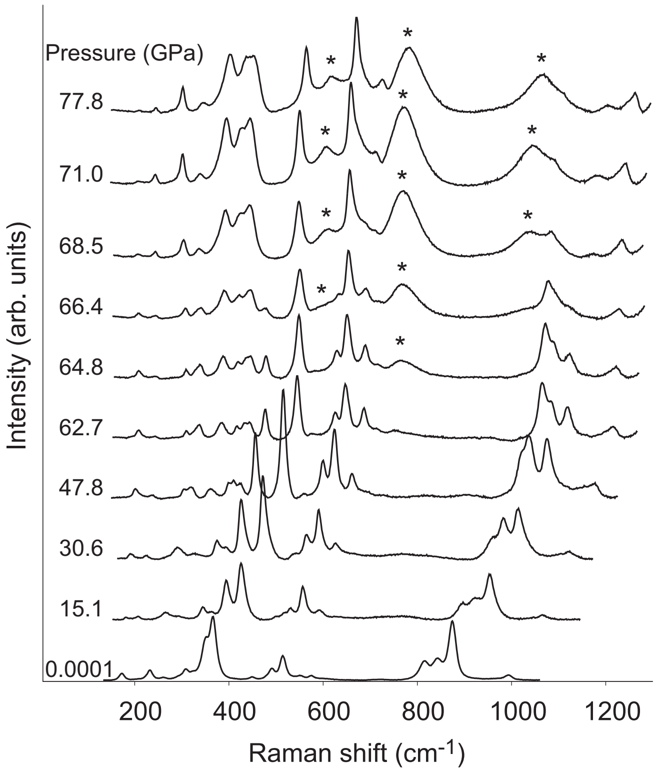

FIG. 6. Selected Raman spectra of an andradite single crystal measured on decompression from 77.8 GPa to ambient conditions. At the highest pressures down to 64.8 GPa broad bands (marked by stars) are observed at about 610, 770, and 1050 cm^{-1} in the low-spin phase of andradite.

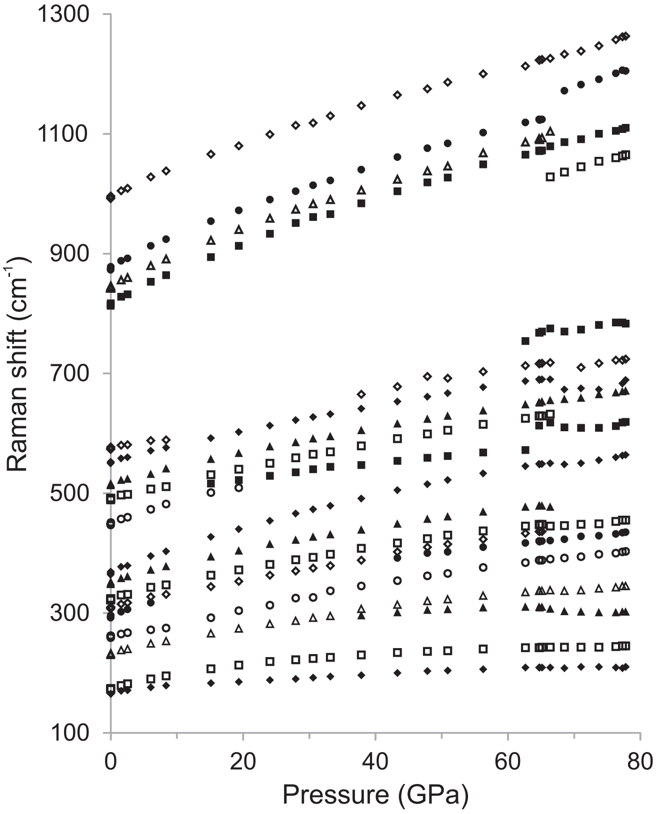

FIG. 7. Pressure-dependent shifts of the Raman modes of andradite with 7 mole% skiagite component measured on decompression from 77.8 GPa to ambient conditions.

assign these three bands. They are significantly broader than the bands due to phonons, and currently we believe that they do not originate from the lattice dynamics. However, calculations to identify if they stem from electronic transitions were beyond the scope of the present study. The vibrational properties of andradite have been extensively studied at ambient pressures by experiment [39,40] and theory [41], and experimentally at high pressure up to 22 GPa and high temperature up to 1173 K [42]. From the detailed pressure-dependent shifts of the Raman modes the mode Grüneisen parameters γ_i of the HS phase were calculated according to $\gamma_i = (B_0/\nu_{i0})(\partial \nu_i/\partial p)$, where B_0 is the bulk modulus at ambient pressure (GPa), ν is the frequency (cm^{-1}), p is the pressure (GPa), and ν_{i0} is the frequency of the vibrational mode i at ambient pressure (cm^{-1}), with $B_0 = 161$ GPa (Fig. 7). γ_i range between 0.61 and 1.34. See Supplemental Material [32] for a detailed table of the pressure-dependent shifts of the Raman modes of andradite and their Grüneisen parameters. While the pressure dependence of the vibrational frequencies is nearly linear in the HS phase, anomalies are observed across the spin transition between 62 and 70 GPa (Fig. 7). As all Raman modes remain observable across the HS-LS transition and in the LS phase, there is no indication for a transition to a metallic state such as was observed by a vanishing of the Raman modes at the Mott transition in CaFe$_2$O$_4$ [43].

The DFT calculations converged to ferromagnetic ground state structures. A population analysis for the HS phases yielded a nominal spin for each Fe^{3+} of 2.04 $\hbar$, i.e., about

80% of the ideal value of $5\times\frac{1}{2}\hbar$. This was independent of pressure. For the LS structures, the population analysis gave 0.44 $\hbar$, close to 90% of the expected ideal value of $\frac{1}{2}\hbar$. Again, there was no pressure dependence of this spin population and no intermediate values were observed in the DFT calculations.

DFT calculations allow us to compute the spin-pairing energy (SPE). For this, we first compute the ground state energy of a fully geometry-optimized structure. Then we fix all structural parameters and recompute the ground state energy by a self-consistent total energy calculation in which the ions are constrained to be in a low-spin state. The difference between these two energies (ΔE) is -1.16 eV/Fe^{3+} ion. Fe^{3+} is a d^5 ion, which in the high-spin state contributes no crystal-field stabilization energy, as the energy gain relative to the field-free ion of the three unpaired electrons in the t_{2g} state is $-3 \times 0.4 \times 10Dq$, while the relative energy cost of occupying the e_g state with two unpaired electrons is $+2 \times 0.6 \times 10Dq$. The energy difference between the two states we calculated is $\Delta E = -20Dq$ + SPE. For andradite $10Dq \approx 1.5$ eV [44,45], and hence the SPE = 4.16 eV, which corresponds to 33553 cm^{-1}. This is in reasonable agreement with the SPE value of 29875 cm^{-1} for the field-free ion [46]. DFT calculations such as those performed here suffer from well-known shortcomings regarding the computation of energies of excited states, and hence the accuracy of the value for the SPE obtained here needs to be confirmed by further calculations, e.g., by time-dependent DFT calculations. Such calculations are currently being performed.

D. Compressibility

The pressure dependencies of the overall and polyhedral volumes of andradite from experiment and theory were fitted to third- and second-order Birch-Murnaghan (BM) equations-of-state, respectively, using the least-squares method and the program EosFit [47]. Experimental p-V data were restricted to pressures of up to 55.5 GPa for the fit to the HS phase, and were weighted with the experimental errors of the pressures and of the volumes only for the overall bulk modulus. Fits to the DFT data were performed in the whole pressure range from 0–80 GPa for both the HS and LS phase. Results are compared to literature data in Table II.

The experimentally determined overall bulk modulus is similar to the literature values of andradite within standard deviation (Table II). The values for the polyhedral bulk moduli obtained in this study seem to be more reliable than those reported by Hazen and Finger [13] as concluded from the excellent agreement with the results from DFT calculations. This is not surprising, as the data by Hazen and Finger [13] were collected using a laboratory x-ray source, which has much less intensity and a much larger beam divergence than the brilliant synchrotron radiation and allows less access to the reciprocal space due to the longer wavelength used. Further, an alcohol mixture was used as pressure-transmitting medium in the earlier study, which is much less hydrostatic at pressures above 10 GPa than neon used in this study. Our results clearly reflect the expected high stiffness of the SiO_4 tetrahedron.

IV. DISCUSSION AND CONCLUSION

The isosymmetric transition in andradite is the first solely pressure-induced structural phase transition reported in a silicate garnet so far. A large pressure-induced change of the FeO_6 octahedral volume, as observed in andradite and many other Fe^{3+}-bearing compounds, may not only be associated with a HS-LS transition but also due to a Mott transition. A simultaneous moment collapse, volume collapse, and metallization transition would result in a direct transition from the high-spin to a zero-spin state, avoiding the low-spin state, and was reported for $CaFe_2O_4$ [43]. However, the transition of andradite at high pressure is clearly not associated with an insulator-metal transition concurrent with a collapse of the magnetic moment as the andradite crystals remain optically transparent. A transition into a metallic state would lead to an opaque sample. Further, the Raman bands remain observable across the spin transition, whereas they would probably vanish in the case of a metallic state. Hence, the spin transition in andradite is not due to a Mott transition but is clearly associated to a HS-LS transition.

Table III gives a summary of spin transitions observed experimentally in Fe^{3+} of octahedral oxygen coordination within oxides. For most of the compounds noble gases (He, Ne, or Ar) were used as pressure-transmitting media for at least part of the experiments and transition pressures given within Table III refer to these experiments. No pressure medium was used in the study of ε-FeOOH [36], and polyethyl siloxane fluid (PES-5) was used in the cases of $Y_3Fe_5O_{12}$ garnet [7,9] and $NdFeO_3$ perovskite [49]. It is well known that the use of nonhydrostatic pressure media can have a significant effect on the evolution of high-pressure phases such as in $CuGeO_3$ [50], or may shift the occurrence of phase transitions to lower pressures due to the presence of deviatoric stresses such as in ZnO, AlN [51], and $MnWO_4$ [52]. The influence of different pressure media on the pressure of the spin transition is discussed within the studies where more than one pressure media were used [43,53–56] but generally is in the range of up to a few GPa for these compounds. Combinations of different experimental methods were used in the studies summarized in Table III, including powder and single-crystal x-ray diffraction, Raman and x-ray emission spectroscopy, conventional and synchrotron Mössbauer spectroscopy, nuclear forward scattering, optical absorption, and electrical resistance measurements, which were accompanied by model calculations in some cases.

The pressure-induced HS-LS transition of Fe^{3+} in andradite occurs at relatively high pressure, commencing at about 60 GPa and is completed at about 70 GPa, if compared to the pressure-induced spin transitions observed in many other Fe^{3+}-bearing oxides (Table III). While iron is only present as Fe^{3+} in octahedral coordination in andradite, both Fe^{2+} and Fe^{3+} are present on the octahedral B site in iron-bearing magnesium silicate perovskites. This complicates the interpretation of Mössbauer spectra in the silicate perovskites [10] and different spin transition pressures of 13–20 GPa [11] and 50–60 GPa [12] were reported for Fe^{3+} on the B site. We can use andradite as a benchmark for the spin-pairing behavior of Fe^{3+} in octahedral coordination in silicates and compare the spin transition pressure of Fe^{3+} in andradite with those reported

TABLE III. Spin transitions observed in Fe^{3+} of octahedral coordination within oxides. s.s. is site symmetry; In-Semi is insulator-to-semiconductor; H-symm. is hydrogen-bond symmetrization. ${}^*Fe^{3+}$ in tetrahedral coordination.

Compound	p (GPa)	B (GPa)	space group	Fe^{3+} s.s.	ΔV (%)	V_{FeO_6}/V (%)	transition types
$Ca_3Fe_2[SiO_4]_3$, andradite, this study	60–70	161(3)	$Ia\bar{3}d$	$\bar{3}$	2.5	10	HS/LS
$(Mg_{0.88}Fe_{0.13})(Al_{0.11}Si_{0.88})O_3$ [57]	70–83	244(3)	$Pbnm$	$\bar{1}$	1.5	<1	HS/LS
$(Mg_{1-x}Fe_x)SiO_3$ perovskite [12]	50–60	237(2)	$Pbnm$	$\bar{1}$	<error	<1	HS/LS
$(Mg_{0.9}Fe_{0.1})SiO_3$ perovskite [11]	13–24		$Pbnm$	$\bar{1}$			HS/LS
$MgSi_{1.5}Fe_{0.15}Al_{0.32}H_{2.6}O_6$, phase D [58]	40–65	147(2)	$P\bar{3}1m$	3.2	3.5	1.4	HS/LS
Fe_2O_3, hematite [3,4,59]	54 [59]/42–58 [3,4]	201(4)	$R\bar{3}c$	3	10	43	HS/LS [4], Mott [3]
ε-FeOOH [36]	53(2)	124(4)	$P2_1nm$	m	11	34	HS/LS, H-symm.
α-FeOOH, goethite [56]	45	120(3)/140(5)	$Pnma$	m	12	31	HS/LS, H-symm.
$CaFe_2O_4$ spinel [43,60]	50	159(2)	$Pbnm$	m,m	8.4	30	HS/LS, Mott [43]
$Y_3Fe_5O_{12}$, garnet-type [7,9]	48(2)	193(4)	$Ia\bar{3}d$	$\bar{3}$, $\bar{4}^*$			HS/LS, Mott [8]
$BiFeO_3$ [54,55,61]	45–55	76(16)	$R3c/Pnma$	$3/m$	5	17.5	HS/LS, Mott [8]
$FeBO_3$ [62–67]	46(2)/53(2) [64]	225(25)	$R\bar{3}c$	$\bar{3}$	8.6	25	HS/LS, In-Semi [8]
$GdFe_3(BO_3)_4$ [53,66]	43	160(6)	$R32$	2		16	HS/LS, In-Semi [8]
$LaFeO_3$ perovskite [68,69]	35–50		$Pbnm$	$\bar{1}$	3	17.9	HS/LS, In-Semi [8]
$PrFeO_3$ perovskite [69,70]	35–50	274(5)	$Pbnm$	$\bar{1}$	3–4	18.1	HS/LS, In-Semi [8]
$NdFeO_3$ perovskite [49]	35–45	244(4)	$Pbnm$	$\bar{1}$	4	18.3	HS/LS, In-Semi [8]
$EuFeO_3$ perovskite [70]	50–60	241(2.5)	$Pbnm$	$\bar{1}$	≈ 5	18.8	HS/LS, In-Semi [8]
$LuFeO_3$ perovskite [70]	50–60	241(5)	$Pbnm$	$\bar{1}$	6.5	19.8	HS/LS, In-Semi [8]

for silicate perovskites. Our results then support the finding of Catalli et al. [12], who concluded that the HS-LS transition of Fe^{3+} at the octahedral B site in iron-bearing magnesium silicate perovskite, $(Mg_{1-x}Fe_x)SiO_3$, occurs at 50–60 GPa [12] and at 70–83 GPa in aluminous perovskite [57], and cast doubt on the very low pressure of 13–24 GPa reported for the HS-LS transition of Fe^{3+} on the B site in $(Mg_{0.9}Fe_{0.1})SiO_3$ perovskite by Lin et al. [11] A comparison with the spin-transition pressures of Fe^{3+} in other oxides, with an average range of 45–55 GPa, also shows that a low spin-transition pressure of 13–24 GPa is highly unlikely for Fe^{3+} in octahedral oxygen coordination (Table III).

The possible pressure-induced spin transition in garnet-type $Y_3Fe_5O_{12}$ occurs at a lower pressure than in andradite (Table III). However, this reconstructive phase transition with a proposed increase from fourfold to sixfold coordination on the tetrahedral Fe^{3+} site cannot be directly compared to the isosymmetric transition in andradite. Further, the spin transition in $Y_3Fe_5O_{12}$ was reported to lead to a metallic state (Mott transition) accompanied by a magnetic transition from the ferrimagnetic to nonmagnetic state [7,8]. Mott transitions accompanying the spin transition in Fe^{3+} have also been reported in $BiFeO_3$ [8] and $CaFe_2O_4$ [43], and are in dispute for Fe_2O_3 [3,4], whereas insulator-to-semiconductor transitions at the spin transitions were reported for borates and $RFeO_3$, $R =$ La, Pr, Nd, Eu, Lu, compounds [8,67]. The concomitant occurrence of another electronic transition (e.g., Mott transition) or structural transition (e.g., hydrogen-bond symmetrization in α- and ε-FeOOH) to the HS-LS transition may complicate the comparison of the spin transitions in different compounds (Table III) and may lead to additional volume collapse at the transition.

The reduction of the unit-cell volume across the spin transition is determined by (i) the reduction of the $Fe^{3+}O_6$ octahedral volume and (ii) the Fe^{3+} content or the proportion of the volume occupied by FeO_6 octahedra with respect to the overall unit cell volume. Hence, the overall volume collapse may be relatively small in the case of small Fe^{3+} contents. This is the case for the respective Fe^{3+}-bearing silicates (Table III), whereas compounds with large Fe^{3+} content, where FeO_6 octahedra occupy a significant amount of the unit cell volume, such as Fe_2O_3, the FeOOH phases, $CaFe_2O_4$, and $FeBO_3$ show a large collapse of the unit cell volume as well. This trend between the overall volume collapse and the volume proportion occupied by FeO_6 octahedra within the crystal structure, calculated from data at ambient conditions, is illustrated in Figure 8.

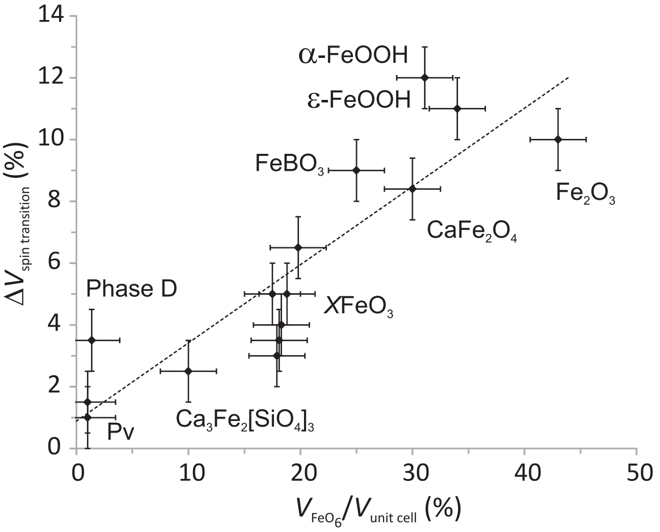

FIG. 8. Dependence of the volume collapse at the spin transition (ΔV) on the volume proportion of FeO_6 octahedra within the unit cell for Fe^{3+}-bearing oxides. For the series $XFeO_3$, $X =$ La, Pr, Nd, Bi, Eu, Lu from bottom to top. Estimated errors are plotted for all data. A linear regression to the data is plotted as a dashed line.

There is no obvious relation between the pressure of the spin transition and the overall bulk modulus (Table III). However, a relationship with the FeO_6 octahedral bulk modulus may be expected. In principle, the FeO_6 bulk modulus should not vary much between different oxides and hence, similar spin transition pressures are expected. Nevertheless, variations of the starting pressures of the spin transitions between about 35 GPa and 60 GPa are observed (Table III). Clearly, data are missing for the bulk modulus of FeO_6 of most compounds. Another measure for the occurrence of a spin transition in Fe^{3+} is the pressure-induced reduction of the Fe–O bond lengths [59]. If the Fe–O distance is reduced below a critical value, the occurrence of a spin transition and the discontinuous reduction of the Fe–O bond length due to the smaller ionic radius of Fe^{3+} in the LS state if compared to the HS state is expected. From the comparison of the reduction of the average Fe–O distances in hematite (α-Fe_2O_3), $CaFe_2O_4$, goethite (α-FeOOH), and $FeBO_3$ as given in Bykova et al. [59], a critical Fe–O distance of below 1.89–1.92 Å is estimated to induce a spin transition in these compounds. This is supported by our findings, where the critical Fe–O distance is 1.88 Å at 60 GPa in andradite (Table I). Therefore, the Fe–O distance of ≈1.9 Å seems to be a critical parameter for all Fe^{3+} sites in octahedral oxygen coordination. Clearly, more structural data of other ferric compounds are needed. In summary, we have identified and characterized a HS-LS transition in Fe^{3+} in andradite, representative for the behavior of Fe^{3+} in octahedral coordination in silicates.

ACKNOWLEDGMENTS

Financial support from the DFG, Germany, within priority program SPP1236 to A.F. (Project FR-2491/2-1) and to B.W. (Project Wi1232/36), the BMBF, Germany (Projects 05KS7RF1, 05K10RFA and 05K13RF1), and DESY-Photon Science, Germany is gratefully acknowledged. Portions of this research were carried out at the light source PETRA III at DESY and at the infrared beam line, IRIS, at BESSY II, both members of the Helmholtz Association (HGF). J.R.-F. thanks the Alexander von Humboldt Foundation for a postdoctoral fellowship. We would like to thank H.-P. Liermann (PETRA III) for assistance in using beamline P02.2 and Ulrich Schade (BESSY II) for support during the measurements. We are grateful for constructive reviews of two anonymous referees that helped to strengthen and improve the manuscript.

---

[1] W. S. Fyfe, Geochim. Cosmochim. Acta **19**, 141 (1960).
[2] M. P. Pasternak, R. D. Taylor, R. Jeanloz, X. Li, J. H. Nguyen, and C. A. McCammon, Phys. Rev. Lett. **79**, 5046 (1997).
[3] M. P. Pasternak, G. K. Rozenberg, G. Y. Machavariani, O. Naaman, R. D. Taylor, and R. Jeanloz, Phys. Rev. Lett. **82**, 4663 (1999).
[4] J. Badro, G. Fiquet, V. V. Struzhkin, M. Somayazulu, H.-k. Mao, G. Shen, and T. LeBihan, Phys. Rev. Lett. **89**, 205504 (2002).
[5] J.-P. Rueff, C.-C. Kao, V. V. Struzhkin, J. Badro, J. Shu, R. J. Hemley, and H. K. Mao, Phys. Rev. Lett. **82**, 3284 (1999).
[6] C. A. Geiger, Elements **9**, 447 (2013).
[7] I. S. Lyubutin, A. G. Gavriliuk, I. A. Trojan, and R. A. Sadykov, JETP Lett. **82**, 702 (2005).
[8] I. S. Lyubutin, S. G. Ovchinnikov, A. G. Gavriliuk, and V. V. Struzhkin, Phys. Rev. B **79**, 085125 (2009).
[9] A. G. Gavriliuk, V. V. Struzhkin, I. S. Lyubutin, M. I. Eremets, I. A. Trojan, and V. V. Artemov, JETP Lett. **83**, 37 (2006).
[10] J.-F. Lin, S. Speziale, Z. Mao, and H. Marquardt, Rev. Geophys. **51**, 244 (2013).
[11] J.-F. Lin, E. E. Alp, Z. Mao, T. Inoue, C. McCammon, Y. Xiao, P. Chow, and J. Zhao, Am. Mineral. **97**, 592 (2012).
[12] K. Catalli, S.-H. Shim, V. B. Prakapenka, J. Zhao, W. Sturhahn, P. Chow, Y. Xiao, H. Liu, H. Cynn, and W. J. Evans, Earth and Planet. Sci. Lett. **289**, 68 (2010).
[13] R. M. Hazen and L. W. Finger, Am. Mineral. **74**, 352 (1989).
[14] L. Zhang, H. Ahsbahs, A. Kutoglu, and C. A. Geiger, Phys. Chem. Minerals **27**, 52 (1999).
[15] Z. Wang, T. Yage, and T. Kondo, J. Phys. Chem. Solids **60**, 441 (1999).
[16] A. Pavese, D. Levy, and V. Pischedda, Eur. J. Mineral. **13**, 929 (2001).
[17] A. Pavese, V. Diella, V. Pischedda, M. Merli, R. Bocchio, and M. Mezouar, Phys. Chem. Minerals **28**, 242 (2001).
[18] M. Koch-Müller, D. Rhede, R. Schulz, and R. Wirth, Phys. Chem. Minerals **36**, 329 (2009).
[19] D. R. Bell, P. H. Ihinger, and G. R. Rossman, Am. Mineral. **80**, 465 (1995).
[20] H. K. Mao, J. Xu, and P. M. Bell, J. Geophys. Res. **91**, 4673 (1986).
[21] R. Boehler, Rev. Sci. Instrum. **77**, 115103 (2006).
[22] H.-P. Liermann, W. Morgenroth, A. Ehnes, A. Berghäuser, B. Winkler, H. Franz, and E. Weckert, J. Phys. Conf. Ser. **215**, 012029/1 (2010).
[23] A. Rothkirch, G. D. Gatta, M. Meyer, S. Merkel, M. Merlini, and H.-P. Liermann, J. Synchrotron Rad. **20**, 711 (2013).
[24] Agilent, CrysAlis^{Pro} *Software System, version 1.171.36.28*, Agilent Technologies UK Ltd., Oxford, UK (2013).
[25] G. M. Sheldrick, Acta Crystallogr. A **64**, 112 (2008).
[26] L. J. Farrugia, J. Appl. Cryst. **32**, 837 (1999).
[27] T. Balić-Žunić and I. Vickovic, J. Appl. Cryst. **29**, 305 (1996).
[28] K. Syassen, *DATLAB* (2005), Version 1.37d, MPI/FKF Stuttgart, Germany.
[29] S. J. Clark, M. D. Segall, C. J. Pickard, P. J. Hasnip, M. I. J. Probert, K. Refson, and M. C. Payne, Z. Kristallogr. **220**, 567 (2005).
[30] H. J. Monkhorst and J. D. Pack, Phys. Rev. B **13**, 5188 (1976).
[31] Z. Wu and R. E. Cohen, Phys. Rev. B **73**, 235116 (2006).
[32] See Supplemental Material at http://link.aps.org/supplemental/10.1103/PhysRevB.90.094105 for a table of the results from electron microprobe analyses and for a detailed table of the pressure-dependent shifts of the Raman modes of andradite and their Grüneisen parameters.
[33] G. Amthauer and G. R. Rossman, Am. Mineral. **83**, 835 (1998).

[34] B. Phichaikamjornwut, H. Skogby, P. Ounchanum, P. Limtrakun, and A. Boonsoong, Eur. J. Mineral. **24**, 107 (2012).

[35] R. Wentzcovitch, H. Hsu, and K. Umemoto, Eur. J. Mineral. **24**, 851 (2012).

[36] A. E. Gleason, C. E. Quiroga, A. Suzuki, R. Pentcheva, and W. L. Mao, Earth and Planet. Sci. Lett. **379**, 49 (2013).

[37] E. V. Akhmatskaya, R. H. Nobes, V. Milman, and B. Winkler, Z. Kristallogr. **214**, 808 (1999).

[38] V. Milman, E. V. Akhmatskaya, R. H. Nobes, B. Winkler, C. J. Pickard, and J. A. White, Acta Crystallogr. B **57**, 163 (2001).

[39] A. M. Hofmeister and A. Chopelas, Phys. Chem. Minerals **17**, 503 (1991).

[40] B. A. Kolesov and C. A. Geiger, Phys. Chem. Minerals **25**, 142 (1998).

[41] F. Pascale, M. Catti, A. Damin, R. Orlando, V. R. Saunders, and R. Dovesi, J. Phys. Chem. B **109**, 18522 (2005).

[42] P. Gillet, G. Fiquet, J. M. Malézieux, and C. A. Geiger, Eur. J. Mineral. **4**, 651 (1992).

[43] E. Greenberg, G. K. Rozenberg, W. Xu, M. P. Pasternak, C. McCammon, K. Glazyrin, and L. S. Dubrovinsky, Phys. Rev. B **88**, 214109 (2013).

[44] D. T. Sviridov, R. K. Sviridova, and J. F. Smirnov, *Optical Spectra of Transition Metal Ions in Crystals* (Nauka, Moscow, 1976).

[45] M.-A. Arrio, S. Rossano, C. Brouder, L. Galoisy, and G. Calas, Europhys. Lett. **51**, 454 (2000).

[46] R. G. Burns, *Mineralogical applications of crystal field theory* (Cambridge University Press, Cambridge, 1993).

[47] R. J. Angel, J. Gonzalez-Platas, and M. Alvaro, Z. Kristallogr. **229**, 405 (2014).

[48] A. B. Woodland, R. J. Angel, M. Koch, M. Kunz, and R. Miletich, J. Geophys. Res. **104**, 20049 (1999).

[49] A. G. Gavriliuk, I. A. Troyan, R. Boehler, M. I. Eremets, I. S. Lyubutin, and N. R. Serebryanaya, JETP Lett. **77**, 619 (2003).

[50] A. Jayaraman, S. R. Shieh, S. K. Sharma, L. C. Ming, and S. Y. Wang, J. Raman Spectr. **32**, 167 (2001).

[51] L. Bayarjargal, L. Wiehl, and B. Winkler, High Press. Res. **33**, 642 (2013).

[52] J. Ruiz-Fuertes, D. Errandonea, O. Gomis, A. Friedrich, and F. J. Manjón, J. Appl. Phys. **115**, 043510 (2014).

[53] I. S. Lyubutin, A. G. Gavriliuk, V. V. Struzhkin, S. G. Ovchinnikov, S. A. Kharlamova, L. N. Bezmaternykh, M. Hu, and P. Chow, JETP Lett. **84**, 518 (2007).

[54] A. G. Gavriliuk, V. V. Struzhkin, I. S. Lyubutin, S. G. Ovchinnikov, M. Y. Hu, and P. Chow, Phys. Rev. B **77**, 155112 (2008).

[55] M. Guennou, P. Bouvier, G. S. Chen, B. Dkhil, R. Haumont, G. Garbarino, and J. Kreisel, Phys. Rev. B **84**, 174107 (2011).

[56] W. Xu, E. Greenberg, G. K. Rozenberg, M. P. Pasternak, E. Bykova, T. Boffa-Ballaran, L. Dubrovinsky, V. Prakapenka, M. Hanfland, O. Y. Vekilova, S. I. Simak, and I. A. Abrikosov, Phys. Rev. Lett. **111**, 175501 (2013).

[57] K. Catalli, S.-H. Shim, P. Dera, V. B. Prakapenka, J. Zhao, W. Sturhahn, P. Chow, Y. Xiao, H. Cynn, and W. J. Evans, Earth Planet. Sci. Lett. **310**, 293 (2011).

[58] Y.-Y. Chang, S. D. Jacobsen, J.-F. Lin, C. R. Bina, S.-M. Thomas, J. Wu, G. Shen, Y. Xiao, P. Chow, D. J. Frost, C. A. McCammon, and P. Dera, Earth Planet. Sci. Lett. **382**, 1 (2013).

[59] E. Bykova, M. Bykov, V. Prakapenka, Z. Konôpková, H.-P. Liermann, N. Dubrovinskaia, and L. Dubrovinsky, High Press. Res. **33**, 534 (2013).

[60] M. Merlini, M. Hanfland, M. Gemmi, S. Huotari, L. Simonelli, and P. Strobel, Am. Mineral. **95**, 200 (2010).

[61] A. G. Gavriliuk, V. V. Struzhkin, I. S. Lyubutin, and I. A. Troyan, JETP Lett. **86**, 197 (2007).

[62] I. A. Troyan, A. G. Gavrilyuk, V. A. Sarkisyan, I. S. Lyubutin, R. Rüffer, O. Leupold, A. Barla, B. Doyle, and A. I. Chumakov, JETP Lett. **74**, 24 (2001).

[63] V. A. Sarkisyan, I. A. Troyan, I. S. Lyubutin, A. G. Gavrilyuk, and A. F. Kashuba, JETP Lett. **76**, 664 (2002).

[64] A. G. Gavriliuk, I. A. Trojan, R. Boehler, M. Eremets, A. Zerr, I. S. Lyubutin, and V. A. Sarkisyan, JETP Lett. **75**, 23 (2002).

[65] I. A. Troyan, M. I. Eremets, A. G. Gavrilyuk, I. S. Lyubutin, and V. A. Sarkisyan, JETP Lett. **78**, 13 (2003).

[66] A. G. Gavriliuk, S. A. Kharlamova, I. S. Lyubutin, I. A. Troyan, S. G. Ovchinnikov, A. M. Potseluiko, M. I. Eremets, and R. Boehler, JETP Lett. **80**, 426 (2004).

[67] I. A. Troyan, A. G. Gavrilyuk, S. G. Ovchinnikov, I. S. Lyubutin, and N. V. Kazak, JETP Lett. **94**, 748 (2012).

[68] G. R. Hearne, M. P. Pasternak, R. D. Taylor, and P. Lacorre, Phys. Rev. B **51**, 11495 (1995).

[69] W. M. Xu, O. Naaman, G. K. Rozenberg, M. P. Pasternak, and R. D. Taylor, Phys. Rev. B **64**, 094411 (2001).

[70] G. K. Rozenberg, M. P. Pasternak, W. M. Xu, L. S. Dubrovinsky, S. Carlson, and R. D. Taylor, Europhys. Lett. **71**, 228 (2005).